IEEE Access
Multidisciplinary | Rapid Review | Open Access Journal

Received 31 August 2022, accepted 26 October 2022, date of publication 1 November 2022, date of current version 11 November 2022.

Digital Object Identifier 10.1109/ACCESS.2022.3218716

RESEARCH ARTICLE

Balance Control of SOC for MMC-BESS With Power Fluctuation Suppression, PCC Voltage Regulation, and Harmonic Mitigation in Grid-Connected Wind Farm

HUI LUO[1], CHEN XU[2], (Member, IEEE), KE DAI[1], CONGZHI CHENG[3], YONGSHUO HUANG[4], AND FEI PAN[5]

[1]State Key Laboratory of Advanced Electromagnetic Engineering and Technology, School of Electrical and Electronic Engineering, Huazhong University of Science and Technology, Wuhan 430074, China
[2]Department of Electrical Engineering, School of Mechatronic Engineering and Automation, Shanghai University, Shanghai 200444, China
[3]Huawei Technologies Company Ltd., Shenzhen 518000, China
[4]Nanning Power Supply Bureau of Guangxi Power Grid Company Ltd., Nanning 530023, China
[5]Shanghai Surpass Sun Electric Company Ltd., Shanghai 200331, China

Corresponding author: Ke Dai (daike@hust.edu.cn)

This work was supported by the National Natural Science Foundation of China under Grant 51807073.

ABSTRACT With the rapid increase in the penetration rate of renewable energy, the power quality of grid-connected wind farm is deteriorated seriously with power fluctuation and point of common coupling (PCC) voltage instability. The conventional solution is to use the energy storage device and the reactive power compensation apparatus to adjust separately, which complicates the system structure. Besides, an active power filter is needed additionally when harmonic pollution caused by local nonlinear load is serious. To solve these problems, this paper investigates the modular multilevel converter-based battery energy storage system (MMC-BESS), which can realize fluctuating power suppression, PCC voltage regulation, and harmonic mitigation simultaneously in grid-connected wind farm. Firstly, the topology and energy flow of MMC-BESS have been studied. Then, three-layer balance control of the state of charge (SOC) is proposed, which is essential to maintaining the normal operation of the device. Finally, the overall control of MMC-BESS applied in the grid-connected wind farm is given. Plenty of experimental results are obtained from a downscaled MMC-BESS prototype, which validate the effectiveness of the proposed control strategy.

INDEX TERMS Modular multilevel converter, battery energy storage system, state of charge, fluctuating power suppression, PCC voltage regulation, harmonic, balance control, wind farm.

I. INTRODUCTION

Nowadays, due to the depleting of fossil energy, clean and renewable energy such as photovoltaics and wind power has been developed and utilized on a large scale [1], [2]. However, with the penetration rate of renewable energy increasing rapidly, the power quality of the power system is deteriorated seriously by fluctuating power and unstable PCC voltage aroused from renewable power [3], [4].

Taking wind power generation as an example, the output power of wind turbines depends on wind speed [5]. Due to the randomness and high uncertainty of wind speed, the output power of wind turbines fluctuates greatly. Besides, with the sudden switching on/off of local loads, the PCC voltage in the grid-connected wind farm is also unstable. Furthermore, the harmonic pollution of local nonlinear loads is another issue that needs to be solved. Currently, the commonly used method in industry is to adjust power fluctuation and PCC voltage through energy storage devices and reactive power compensation equipment separately.

The associate editor coordinating the review of this manuscript and approving it for publication was Alexander Micallef.

In order to smoothen the output power of the wind farm, supercapacitors and flywheel energy storage devices can be used to achieve power fluctuation suppression [6], [7]. However, their energy storage density is limited, so they become costly in suppressing large-scale power fluctuation. Therefore, the hybrid energy storage device was proposed [8], [9], in which, wind farm power is divided into three parts. The high-frequency part with fast fluctuation is suppressed by supercapacitors, the intermediate-frequency part with slightly smooth fluctuation is suppressed by the batteries, and the low-frequency part with relatively flat fluctuation amplitude is used as the grid-connected power. Thus, the fluctuating power of the wind farm is eventually suppressed by the hybrid energy storage device. Although the methods above overcome the shortcoming of the low power density of a single energy storage device, its coordinated control strategy is more complicated. If the grid-connected wind farm still needs to stabilize the PCC voltage or suppress harmonics at the same time, additional installation of a static var compensator (SVC) or harmonic treatment device is necessary. However, it needs extra expense and makes the system structure more complicated [10].

Compared with the conventional two-level/three-level converters, the multilevel structure is preferable in high voltage and high power applications [11]. The modular multilevel converter (MMC) is a more promising topology than the neutral point clamped (NPC) converter, flying capacitor converter (FCC), and cascaded H-bridge converter (CHB). Because MMC has the advantages of simple control, good modularity, superior scalability, high efficiency, and lower output voltage total harmonic distortion (THD) [12], [13], [14]. When the battery energy storage system (BESS) is combined with MMC, the capability of reactive power compensation of BESS can be expanded. Moreover, it can achieve active and reactive power regulation in one device at the same time. That means it can solve the problems of output power and PCC voltage fluctuation in the wind farm, which tends to have good economic performance compared with adjusting the power fluctuation and PCC voltage through energy storage devices and reactive power compensation equipment separately. Besides, by controlling the output current of the MMC-BESS to mitigate the harmonic current generated by local nonlinear loads, the power quality of the grid-connected wind farm can be further improved.

Since Trintis et al. proposed the modular multilevel converter-based battery energy storage system (MMC-BESS) in 2011 [15], the novel topology has drawn a lot of attention among researchers [16], [17], [18], [19], [20], [21], [22]. Generally, the energy storage unit of MMC has two access methods [17], [18]. The first is that a large quantity of energy storage units is connected to the DC bus in series and parallel [19]. The second is that the energy storage unit is distributed to each submodule directly or through a non-isolated DC/DC converter. The latter is more popular than the former as it has the advantages of flexible control and strong fault tolerance, which is critical in high voltage and large capacity applications [20], [21], [22]. During the operation of MMC-BESS, the state of charge (SOC) of the energy storage unit in each submodule will differ from each other due to the aging degrees of the battery [23]. In order to improve the utilization of battery capacity, the balance control of SOC is indispensable and is a key control technology of MMC-BESS.

This paper investigates the control strategy of MMC-BESS, which can comprehensively realize power fluctuation suppression, PCC voltage regulation, and harmonic mitigation in wind farm. Simultaneously, three-layer balance control of SOC is proposed, which is essential to maintaining the normal operation of MMC-BESS. Compared with the SOC balance control presented in [17] and [18], the three-layer balance control of SOC proposed in this paper is realized by regulating the DC and fundamental component of circulating current directly, reconstructing the modulation wave respectively, which is simple and effective. The rest of this paper is composed of five parts. Section II gives the topology of MMC-BESS and then analyzes the energy flow of the whole device. Section III introduces the three-layer balance control of SOC in detail. The overall control of MMC-BESS including fluctuating power suppression, PCC voltage regulation, and harmonic mitigation in the grid-connected wind farm is illustrated in Section IV. Plenty of experimental results are given subsequently in Section V, which verify the effectiveness of the proposed control strategy. Finally, conclusions are drawn in Section VI.

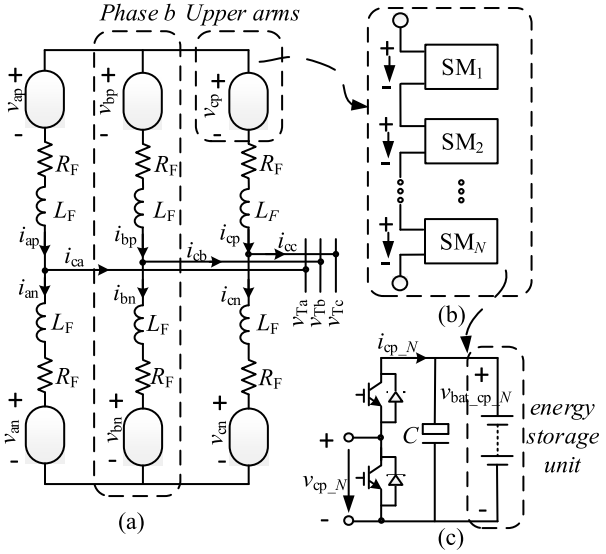

FIGURE 1. Main circuit topology of MMC-BESS.

II. TOPOLOGY AND ENERGY FLOW OF MMC-BESS

A. TOPOLOGY AND MATHEMATICAL MODEL

The main circuit topology of three-phase three-wire MMC-BESS is shown in Fig.1(a), which is composed of two

star-connected three-phase half-bridge cascaded converters (HBCC) in anti-parallel. Each phase consists of the upper and lower arm, which is formed through N cascaded submodules separately as shown in Fig.1(b). The upper and lower arm is connected to the midpoint of each pole via the buffer inductor and resistor, then the midpoint of the pole is directly connected to the PCC. As described in Fig.1(c), the SM is the half-bridge structure, including two IGBTs with their anti-parallel diodes, and a capacitor connected in parallel on the DC side. At the same time, the energy storage unit which consists of several batteries in series is directly connected to the capacitor in parallel. The output voltage of the AC side of the SM is either equal to its capacitor voltage or zero, depending on the switching states of the two switches. Define the cascaded voltage of N submodules on the upper arm as v_{jp} (j = a, b, c), and the total voltage of the lower arm as v_{jn}. The virtual common DC side voltage is noted as V_{dc}, and the upper and lower arms currents are defined as i_{jp} and i_{jn} (j = a, b, c), respectively. Then denote the output current of the device as i_{cj}, whose positive direction is point to PCC. The PCC voltage is v_{Tj} (j = a, b, c). The buffer inductor is marked as L_F and the resistor as R_F. i_{cp_N} represents the capacitor current of the Nth submodule of the upper arms, whose DC side voltage and AC side voltage are expressed as $v_{bat\_cp\_N}$ and v_{cp_N}, respectively.

According to [24] and [25], equation (1) describes the external characteristics of MMC-BESS, and equation (2) describes the internal voltage and current characteristics.

$$e_{difj} = v_{Tj} + \frac{L_F}{2}\frac{di_{cj}}{dt} + \frac{R_F}{2}i_{cj} \tag{1}$$

$$L_F\frac{di_{cir}}{dt} + R_F i_{cir} = \frac{V_{dc}}{2} - e_{sumj} \tag{2}$$

e_{difj} (j = a, b, c) represents the differential mode voltage that can be used to control the output current of MMC-BESS. e_{sumj} (j = a, b, c) is denoted as the common mode voltage which can be used to control the circulating current as shown in (2). According to formula (1), the equivalent circuit of MMC-BESS is shown in Fig.2.

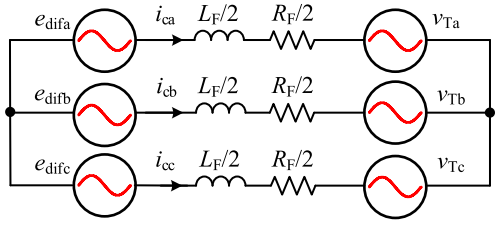

FIGURE 2. Simplified equivalent circuit of MMC-BESS.

B. ENERGY FLOW IN MMC-BESS

Assuming that the modulation wave of the lower arms is $m\sin(\omega t + \theta_j)$ (j = a, b, c), which is inverse to that of the upper arms. The initial phase angle of each phase is $\theta_a = 0$, $\theta_b = -2\pi/3$, $\theta_c = 2\pi/3$.

$$\begin{cases} v_{jp} = \dfrac{\sum_{z=1}^{N} v_{bat\_jp\_z}}{2} - \dfrac{\sum_{z=1}^{N} v_{bat\_jp\_z}\cdot m\sin(\omega t+\theta_j)}{2} \\ \quad = \dfrac{V_{dc}}{2} - \dfrac{V_{dc}}{2}m\sin(\omega t+\theta_j) \\ v_{jn} = \dfrac{\sum_{z=1}^{N} v_{bat\_jn\_z}}{2} + \dfrac{\sum_{z=1}^{N} v_{bat\_jn\_z}\cdot m\sin(\omega t+\theta_j)}{2} \\ \quad = \dfrac{V_{dc}}{2} + \dfrac{V_{dc}}{2}m\sin(\omega t+\theta_j) \end{cases} \tag{3}$$

Under phase-shifted carrier pulse width modulation (PSC-PWM), the total voltage of the upper and lower arms can be expressed by (3), which are both composed of DC and fundamental components.

Since the batteries are connected to the capacitor in parallel directly, the DC side voltage of the submodule is relatively stable. Therefore, the second harmonic component of the AC side current is neglected, which can be expressed by (4)

$$\begin{cases} i_{jp} = I_{cir\_dc} + \dfrac{1}{2}I_{cj}\sin(\omega t+\varphi_j) + \\ I_{cir\_50Hz}\sin(\omega t+\gamma_j) \\ i_{jn} = I_{cir\_dc} - \dfrac{1}{2}I_{cj}\sin(\omega t+\varphi_j) + \\ I_{cir\_50Hz}\sin(\omega t+\gamma_j) \end{cases} \tag{4}$$

where φ_j represents the phase angle of the fundamental component of the output current, and γ_j stands for the phase angle of the fundamental component of the circulating current.

The power of the upper arm, lower arm, and whole phase, marked as P_{jp}, P_{jn}, and P_j (j = a, b, c), is obtained by multiplying (3) and (4), which can be expressed as

$$\begin{cases} P_{jp} = \dfrac{V_{dc}}{2}I_{cir\_dc} - \dfrac{V_{dc}}{4}mI_{cj}\cos(\theta_j-\varphi_j) - \\ \dfrac{V_{dc}}{2}mI_{cir\_50Hz}\cos(\theta_j-\gamma_j) \\ P_{jn} = \dfrac{V_{dc}}{2}I_{cir\_dc} - \dfrac{V_{dc}}{4}mI_{cj}\cos(\theta_j-\varphi_j) + \\ \dfrac{V_{dc}}{2}mI_{cir\_50Hz}\cos(\theta_j-\gamma_j) \\ P_j = V_{dc}I_{cir\_dc} - \dfrac{V_{dc}}{2}mI_{cj}\cos(\theta_j-\varphi_j) \end{cases} \tag{5}$$

It can be seen from (5) that the power of each phase P_j is affected by the DC component of circulating current I_{cir_dc} and the output current of the device I_{cj}. By regulating I_{cir_dc}, P_j can be changed. The power of the arms P_{jp} or P_{jn} is affected by the DC and fundamental component of the circulating current (i.e., I_{cir_dc} and I_{cir_50Hz}) and the output current of the device I_{cj}. However, I_{cir_50Hz} has the opposite effect on P_{jp} and P_{jn}, which means it can be controlled to regulate the power between the upper and lower arm without changing the phase power P_j. The analysis above shows that the circulating current may change the energy flow between different phases as well as between the upper and lower arm. Hence, the SOC balance between different phases, between the upper

and lower arm can be achieved by controlling the circulating current.

III. THREE-LAYER BALANCE CONTROL OF SOC

When MMC-BESS is put into operation and the output power of each submodule is the same, the difference in SOC value between batteries may gradually become larger due to the slight difference between batteries.

The coulomb counting method can be used to estimate the SOC of battery, which is shown as

$$\mathrm{SOC}(t) = \mathrm{SOC}(0) - \frac{\int_0^t i_{jp/jn\_N}(\tau)d\tau}{3600Q_{\max}} \tag{6}$$

where SOC(0) is the initial SOC value of the battery and $Q_{\max}$ represents the maximum charge of the battery.

$$\begin{cases} \mathrm{SOC}_{jp} = (\sum_{i=1}^{N} \mathrm{SOC}_{jp\_i})/N \\ \mathrm{SOC}_{jn} = (\sum_{g=1}^{N} \mathrm{SOC}_{jn\_g})/N \\ \mathrm{SOC}_j = (\mathrm{SOC}_{jp} + \mathrm{SOC}_{jn})/2 \\ \mathrm{SOC}_{abc} = (\mathrm{SOC}_a + \mathrm{SOC}_b + \mathrm{SOC}_c)/3 \end{cases} \tag{7}$$

As shown in (7), SOC_{jp}, SOC_{jn}, and SOC_j are defined as the average SOC value between submodules in the upper arm, lower arm, and whole phase j (j = a, b, c), respectively. SOC_{abc} is the average SOC value of the entire device. The proposed three-layer balance control strategy of SOC for MMC-BESS is illustrated in Fig.3.

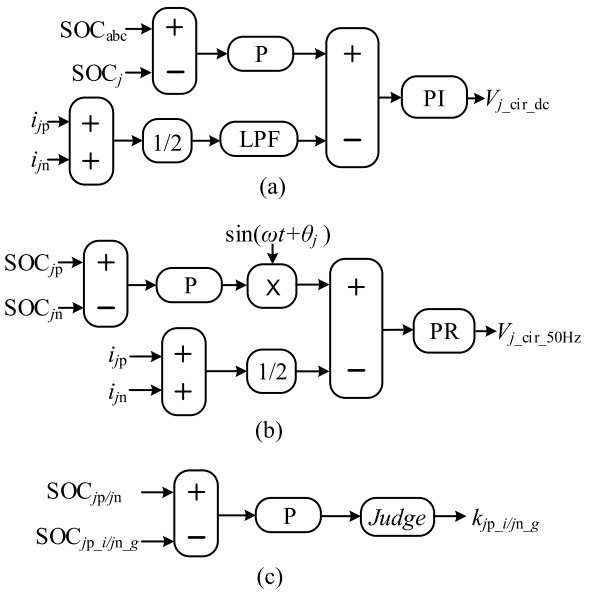

FIGURE 3. Three-layer balance control of SOC. (a) Different poles. (b) Upper and lower arm in the same pole. (c) Submodules in the same arm.

A. SOC BALANCE CONTROL BETWEEN DIFFERENT POLES

According to the previous analysis, the energy between different phases can be distributed to achieve the SOC balance by controlling the DC component of the circulating current $I_{\mathrm{cir\_dc}}$. Hence, the first layer balance control between different poles is shown in Fig.3(a). In Fig.3(a), the average SOC value of each phase is subtracted from the average SOC value of the whole system, then the error is amplified by the proportional controller to obtain the reference of the DC circulating current. Meanwhile, the circulating current is passed through a low-pass filter (LPF) to obtain the feedback value of the DC circulating current. Then the error between the reference and feedback value is sent to the PI controller to obtain the modulation wave $V_{j\_\mathrm{cir\_dc}}$, which can realize the SOC balance control between different poles.

B. SOC BALANCE CONTROL BETWEEN UPPER AND LOWER ARM IN THE SAME POLE

By controlling the fundamental component of the circulating current $I_{\mathrm{cir\_50Hz}}$, the energy between the upper and lower arm in the same pole can be distributed to realize the SOC balance between them without changing the total energy of the pole. The control scheme is illustrated in Fig.3(b). If the fundamental component of the circulating current is positive, the upper arm transfers energy to the lower arm, and vice versa. Therefore, the difference in the average SOC value between the upper and lower arm is amplified by the proportional controller, and the result is used as the amplitude of the fundamental component of the circulating current reference, whose phase is consistent with the PCC voltage. Then the error between the reference and feedback value is adjusted by the proportional resonant (PR) regulator to obtain the modulation wave $V_{j\_\mathrm{cir\_50Hz}}$. Thus, the SOC balance between the upper and lower arm in the same pole can be achieved. The PR regulator is applied to extract the fundamental component of the circulating current, so its resonant frequency is designed at 50Hz.

C. SOC BALANCE CONTROL BETWEEN SUB-MODULES IN THE SAME ARM

Since the submodules in the same arm are connected in series, the energy distribution of these submodules cannot be realized by controlling the circulating current. At this time, reconstructing the modulation wave of each submodule is proposed. As shown in Fig.3(c), the average SOC value between the arm and individual submodule is sent to the proportional controller. Then the result is judged by the Judge function, which is shown in Fig.4(a), to get the modulation factor k_{jp_i/jn_g} of the submodule. In this way, the modulation wave of each submodule in the same arm is reconstructed, which means the energy of each submodule can be distributed. Hence, the SOC balance control between submodules in the same arm can be realized. At this time, on the basis of the balance control in the first two layers, the SOC balance of all submodules can be realized.

The Judge function is employed to extend the working time of the submodule with a relatively small SOC value in the case of charging by amplifying the modulation wave, which means that it can be charged more. Similarly, the working time of

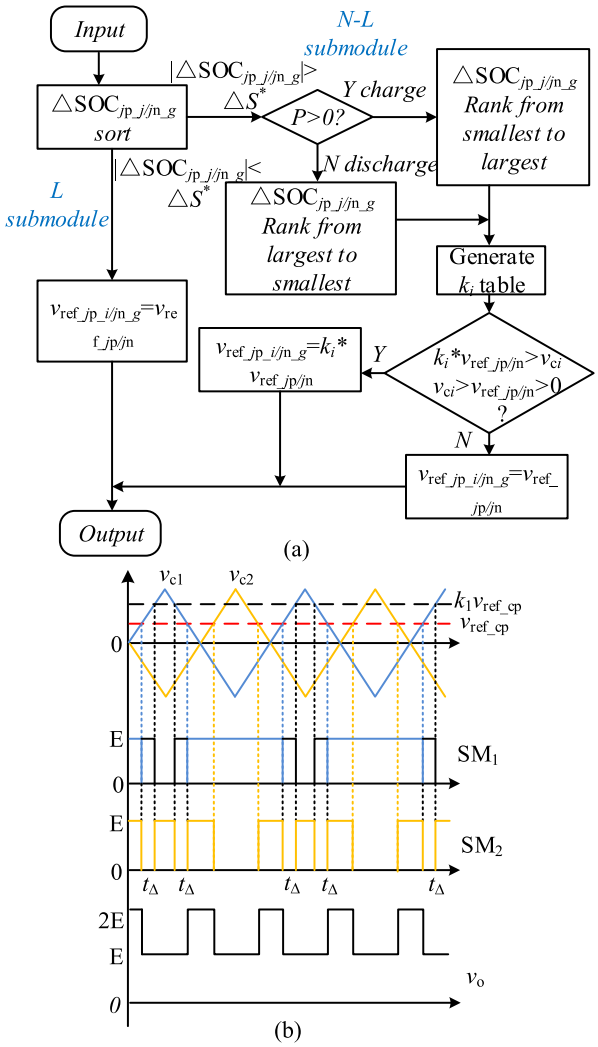

FIGURE 4. Judge function of SOC balance control between submodules in the same arm. (a) Flowchart of judge function (b) PSC-PWM waveform when $N = 2$.

the submodule with a larger SOC value will be increased in the case of discharging to make it discharge more. More importantly, the method above does not change the equivalent output voltage waveform of the arm. When the SOC value of SM_2 is bigger than that of SM_1 and MMC-BESS is charging, the basic principle of reconstructing the modulation wave of PSC-PWM is illustrated in Fig.4(b). As shown in Fig.4(b), when the condition of $k_1 v_{ref\_cp} > v_{c1} > v_{ref\_cp}$ is true, SM_2 is forced to output low level while the final equivalent output voltage of the arm is the same as when both submodules are modulated by v_{ref_cp}. In this way, the SOC of each submodule can be balanced while the harmonics of the equivalent output voltage of the arm are not increasing.

IV. IMPROVEMENT OF POWER QUALITY IN GRID-CONNECTED WIND FARM BY MMC-BESS

A. PCC VOLTAGE AND REACTIVE POWER

As shown in Fig.5(a), a simplified diagram of the grid-connected wind farm is given. The active power output by

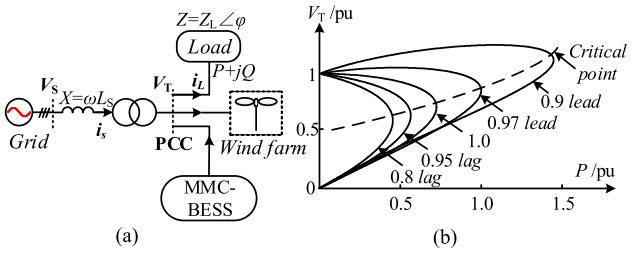

FIGURE 5. The grid-connected wind farm system. (a) Simplified diagram. (b) P-V characteristic nose curve.

the wind farm is greatly determined by wind speed, which has great volatility and randomness. Besides, the sudden change of local load or severe short-circuit fault will cause the PCC voltage to be over/under voltage. Moreover, due to local nonlinear loads, harmonic pollution will occur if it is not treated effectively. Therefore, the power quality in the grid-connected wind farm faces great challenges. In this paper, it is proposed to install MMC-BESS at PCC in parallel near the wind farm to improve the power quality of the system as shown in Fig.5(a).

In order to analyze the characteristic of PCC voltage, the wind farm and MMC-BESS in Fig.5(a) can be considered as a part of the load connected to the grid. Meanwhile, the transformer turns ratio is assumed to be 1:1 and the equivalent resistance of the transmission line is ignored. In this way, the relationship between active power, PCC voltage, and load can be described by (8).

$$\begin{cases} P &= \dfrac{V_S^2 Z_L \cos\varphi}{X^2 + Z_L^2 + 2XZ_L \sin\varphi} \\ V_T &= \dfrac{V_S Z_L}{\sqrt{X^2 + Z_L^2 + 2XZ_L \sin\varphi}} \end{cases} \tag{8}$$

In Eq.(8), V_S is the ideal grid voltage. V_T, X, and Z_L represent the PCC voltage, line impedance, and load impedance, respectively. P stands for the active power of the whole system, whose power factor angle is φ.

Supposing the load is a pure resistor, the maximum active power is given in (9) when the norm of load impedance is equal to the norm of line impedance.

$$P_{max} = \frac{V_S^2}{2X} \tag{9}$$

If the characteristic of load changes, the equations P/P_{max} and V_T/V_S can be derived as follows

$$\begin{cases} \dfrac{P}{P_{max}} &= \dfrac{2XZ_L \cos\varphi}{X^2 + Z_L^2 + 2XZ_L \sin\varphi} \\ \dfrac{V_T}{V_S} &= \dfrac{Z_L}{\sqrt{X^2 + Z_L^2 + 2XZ_L \sin\varphi}} \end{cases} \tag{10}$$

According to (10), by changing the load power factor, the P-V characteristic nose curve of the system can be obtained, which is shown in Fig.5(b). As can be seen from Fig.5(b), the maximum active power varies with the load power factor. The system needs to work in the interval above the critical point.

For resistive-capacitive loads, the maximum active power absorbed by loads is higher than that of purely resistive loads, and the PCC voltage is higher than the grid voltage. If the load appears resistive-inductive, the maximum active power absorbed by loads is lower than that of purely resistive loads situation, and the PCC voltage is lower than the grid voltage. The inductive or capacitive loads will decrease or increase the PCC voltage, deteriorating the power quality of the system.

B. FLUCTUATING POWER SUPPRESSION

Supposed the local load is ignored, the power flow of the grid-connected wind farm can be calculated as

$$P_{\mathrm{g}} = P_{\mathrm{wf}} + P_{\mathrm{mb}} + P_{\mathrm{f}} \tag{11}$$

P_{g} represents the active power absorbed by the grid. P_{wf} is denoted as the active power generated by the wind farm. P_{mb} is expressed as the active power of MMC-BESS, and P_{f} is indicated as the active power loss of the entire system which can be neglected for the reason of a small amount.

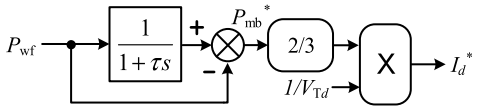

FIGURE 6. Fluctuating power suppression current reference.

The fluctuating active power generated by the wind farm, which varies with wind speed, will weaken the system's stability. Hence, it needs to be smoothed. Since the high-frequency part of the wind farm power is the main suppression target, a first-order low pass filter (LPF) can be used to design the fluctuating power suppression strategy, which is illustrated in Fig.6. The active power output by the wind farm is filtered through a first-order LPF to obtain the expected active power, which is subtracted from the input of the filter to obtain the active power reference P_{mb}^* of MMC-BESS. Then multiply P_{mb}^* by 2/3 and $1/V_{\mathrm{T}d}$ to get the active current reference I_d^* of MMC-BESS. By controlling the active current, MMC-BESS can output active power to counteract the fluctuating power of the wind farm, realizing power fluctuation suppression. Consequently, the grid can obtain relatively stable active power. In Fig.6, $\tau = 1/2\pi f_{\mathrm{L}}$, and f_{L} is the cut-off frequency of the LPF.

C. PCC VOLTAGE REGULATION

If considering the local loads, sudden changes in the load will cause PCC voltage fluctuations. According to the P-V characteristic nose curve shown in Fig.5(b), PCC voltage can be regulated to a specified range by controlling MMC-BESS to inject a certain amount of reactive power into the grid.

As shown in Fig.7, the PCC voltage is detected and sent to the synchronous rotating coordinate firstly, whose d-axis is defined to be coaxial with the three-phase equivalent electromotive force. Then, after the equal amplitude coordinate transformation, the d-axis component of the voltage represents the amplitude of phase voltage of PCC, which

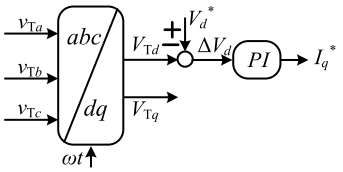

FIGURE 7. PCC voltage regulation current reference.

is subtracted with the reference of the rated amplitude of PCC voltage. Subsequently, the error is regulated by the PI controller to obtain the reference of the q-axis current of MMC-BESS. By controlling the corresponding reactive current, MMC-BESS can inject required reactive power into the grid, realizing over/under voltage regulation.

D. HARMONIC MITIGATION

As shown in Fig.5(a), since local loads in the grid-connected wind farm usually consist of nonlinear loads, it is necessary to suppress harmonic currents generated by the nonlinear loads to avoid harmonic pollution. Compared with installing a harmonic suppression device at PCC additionally, using MMC-BESS for harmonic mitigation is a more economical solution.

In order to achieve harmonic suppression, it is essential to extract the desired harmonics i_{Lk}^* from the nonlinear load current i_L. Among the various selective extraction methods, Recursive Discrete Fourier Transform (RDFT) is the most preferred one due to its low computational burden and fast dynamic time [26], which can be expressed as

$$\begin{aligned} i_{Lh}^* &= \sum_{k=1}^{K_m} \left[A_k(n)\cos(k\omega_1 n\tau) + B_k(n)\sin(k\omega_1 n\tau)\right] \\ &\begin{cases} A_k(n) = A_k(n-1) + \frac{2}{N}\left[i_L(n) - i_L(n-N)\right]\cos(k\omega_1 n\tau) \\ B_k(n) = B_k(n-1) + \frac{2}{N}\left[i_L(n) - i_L(n-N)\right]\sin(k\omega_1 n\tau) \end{cases} \end{aligned} \tag{12}$$

where K_m is the maximum harmonic order to be concerned. A_k and B_k are the cosine and sine amplitudes of k^{th} harmonic. ω_1 is the fundamental angular frequency of the grid. n is the present instant with the discrete cycle τ. N is the number of sampling points in each fundamental cycle T_1, therefore $T_1 = N\tau$.

Based on RDFT, Fig.8 shows the harmonic extraction strategy in the grid-connected wind farm. As can be seen from Fig.8(b), harmonic reference $i_{Lh\alpha\beta}^*$ is the sum of desired harmonics i_{Lk}^*, which are selectively extracted from load current i_L by RDFT_k as shown in Fig.8(a). Then, through $\alpha\beta/dq$ coordinate transformation, the harmonic reference in the dq frame can be obtained, which are marked as $i_{Lh\_d}^*$ and $i_{Lh\_q}^*$. Finally, by the current controller in the dq frame, MMC-BESS can output currents with the same magnitude and direction as the harmonic currents, realizing harmonic mitigation in the grid-connected wind farm.

The overall control architecture of MMC-BESS for the grid-connected wind farm is shown in Fig.9, which includes

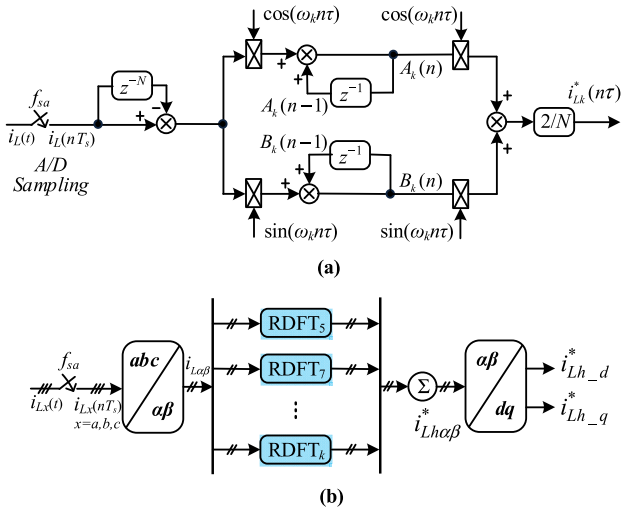

FIGURE 8. Selective harmonic extraction for MMC-BESS with RDFT. (a) RDFT$_k$. (b) Harmonic extraction strategy.

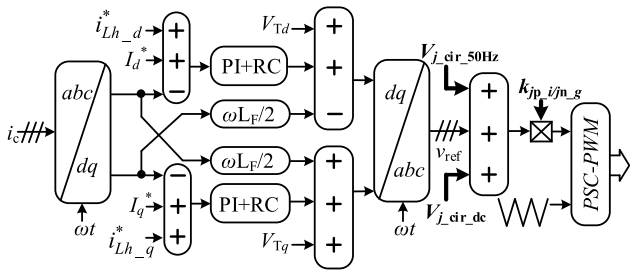

FIGURE 9. Overall control of MMC-BESS for the grid-connected wind farm.

fluctuating power suppression, PCC voltage regulation, harmonic mitigation, and the three-layer balance control of SOC. First, in the synchronous rotating coordinate, the parallel-connected PI controller and repetitive controller (RC) are adopted to track the reference of active currents, reactive currents, and harmonic currents which are obtained from fluctuating power suppression, PCC voltage regulation, and harmonic mitigation control strategy, respectively. Then, due to the coupling of the *d, q* axis current caused by the connected inductance, the state variable feedback cross-decoupling of the *d, q* axis current is carried out. The PCC voltage feedforward is also adopted to improve the dynamic performance of the system. Next, through *dq/abc* coordinate transformation, the output voltage reference v_{ref} in the three-phase stationary coordinate can be obtained. Finally, in order to achieve SOC balance of all submodules, superimposing the modulation reference $V_{j\_\text{cir\_dc}}$ and $V_{j\_\text{cir\_50Hz}}$ on the original reference v_{ref}, and multiplying the result by the proportional coefficient $k_{\text{jp\_}i/\text{jn\_}g}$, the final modulation waves are obtained. Through PSC-PWM, the drive signals are finally got.

V. EXPERIMENTAL VALIDATION

In order to verify the correctness of the proposed control strategy, a three-phase three-wire downscaled laboratory prototype of MMC-BESS is built as shown in Fig.10, whose experimental parameters are given in Table. 1. Each arm consists of two submodules and thus the device has twelve submodules in total.

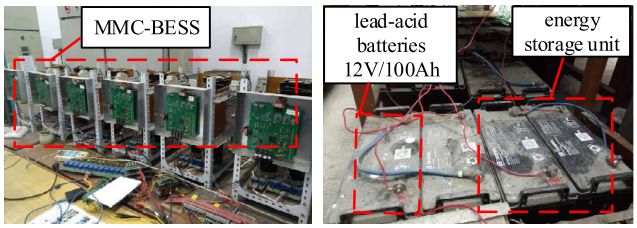

FIGURE 10. Downscaled prototype of MMC-BESS. (a) MMC-BESS. (b) Storage unit on the DC side of submodules.

TABLE 1. Experimental parameters of MMC-BESS.

Quantity	Label	Value
Phase-to-phase voltage (RMS)	V_l/V	20/60
DC side voltage of submodule	E_{SM}/V	24/72
Line inductor	L_g/mH	0.5
Buffer inductor	L_F/mH	5
DC-link capacitor	C/μF	4700
SM number per arm	N	2
Fundamental frequency	f_s/Hz	50
Carrier frequency	f_c/kHz	1
Equivalent switching frequency	f_{sw}/kHz	4
Sampling frequency	f_{sa}/kHz	4
Delta-connected resistor (load A)	R/Ω	24
Star-connected resistor (load B)	R/Ω	24
Star-connected inductor (Load C)	L/mH	6
Three-phase diode rectifier (Load D)	R/Ω	3
	L/mH	0.5

At first, V_l and E_{SM} are set to 20V and 24V respectively when SOC balance control, fluctuating power suppression, and PCC voltage regulation were implemented by MMC-BESS. At this time, the DC side of each submodule is connected with two 12V/100Ah lead-acid batteries in series, which is shown in Fig.10(b). Then, in order to verify the feasibility of the proposed harmonic mitigation strategy further, the DC side of each submodule is connected with their DC-link capacitor only since the number of lead-acid batteries is limited in the laboratory. Accordingly, V_l and E_{SM} are increased to 60V and 72V respectively. It should be noted here that the DC side voltage of each submodule can be conveniently adjusted by changing the number or voltage rating of batteries in practical applications. Similarly, the phase-to-phase voltage can be adjusted by the voltage regulator easily in the laboratory.

Under laboratory conditions, the short-term fluctuating active power of the simulated wind farm is directly generated through the MATLAB random function. As shown in Table.1, load A and load B are switched on/off to simulate under/over voltage in the grid-connected wind farm. A typical three-phase bridge diode rectifier (Load D) is chosen as a nonlinear load, whose DC side is connected with a 3Ω resistor and

0.5mH inductor in series. After applying PSC-PWM, the equivalent switching frequency of the device is 4kHz while the switching frequency of a single submodule is 1kHz. Therefore, the prototype only suppresses the 5th, 7th, and 11th harmonics selectively when the harmonic mitigation strategy was implemented by the prototype due to the limitation of the equivalent switching frequency.

A. SOC BALANCE CONTROL

For simplification, (13) is used to calculate the SOC value of each submodule, where $V_{\text{omax}} = 27\text{V}$ is the maximum open-circuit voltage of the battery, and $V_{\text{omin}} = 18\text{V}$ is the minimum open-circuit voltage of the battery. The initial SOC of the energy storage unit at all layers can be calculated by (7) and (13), and the results are shown in Table.2.

$$\text{SOC} = \frac{V_{\text{bat}} - V_{\text{o min}}}{V_{\text{o max}} - V_{\text{o min}}} \times 100\% \tag{13}$$

TABLE 2. SOC values before and after balance control.

	Storage unit	ap_1	ap_2	an_1	an_2	**ap**	**an**	**a**
before	*voltage*/V	24.13	23.52	18.65	20.22	23.83	19.44	21.63
	SOC/%	68.11	61.33	7.22	24.67	64.72	15.94	40.33
after	*voltage*/V	24.07	23.88	23.42	23.75	23.98	23.59	23.78
	SOC/%	67.44	65.33	60.22	63.89	66.39	62.06	64.23
	Storage unit	bp_1	bp_2	bn_1	bn_2	**bp**	**bn**	**b**
before	*voltage*/V	24.13	23.79	22.81	22.75	23.96	22.78	23.37
	SOC/%	68.11	64.33	53.44	52.78	66.22	53.11	59.67
after	*voltage*/V	24.05	23.94	23.82	23.80	23.99	23.81	23.90
	SOC/%	67.22	66.0	64.67	64.44	66.61	64.56	65.59
	Storage unit	cp_1	cp_2	cn_1	cn_2	**cp**	**cn**	**c**
before	*voltage*/V	18.4	23.7	23.93	23.47	21.05	23.7	22.28
	SOC/%	4.44	63.33	65.89	60.78	33.89	63.33	48.61
after	*voltage*/V	23.38	23.94	23.98	23.87	23.66	23.93	23.79
	SOC/%	59.78	66.0	66.44	65.22	62.89	65.83	64.36

Under ideal equilibrium conditions, the expected SOC value of energy storage units at all layers is 66.67%, and the expected standard deviation of SOC of all submodules is 0. It can be calculated from Table.2 that before SOC balance control is implemented, the average SOC value of the first layer which is among the three phases is 49.54%. The average SOC values of the second layer which is between upper and lower arms in the same phase are 40.33%, 59.67%, and 48.61%, respectively. The average SOC value of all submodules also known as the third layer is 49.54%, whose standard deviation is 23.55. It can be seen that without the three-layer balance control, the SOC of the energy storage unit at all layers is far from the expected value. Simultaneously, the standard deviation of the submodules is large, and the SOC distribution is relatively scattered.

The active power reference of MMC-BESS is set to 110W, while the reactive current reference is set to 0. Thus the MMC-BESS is charging when assuming the positive direction of the grid-connected current is from PCC to MMC-BESS. Fig.11 shows the result when the three-layer balance control is employed during charging.

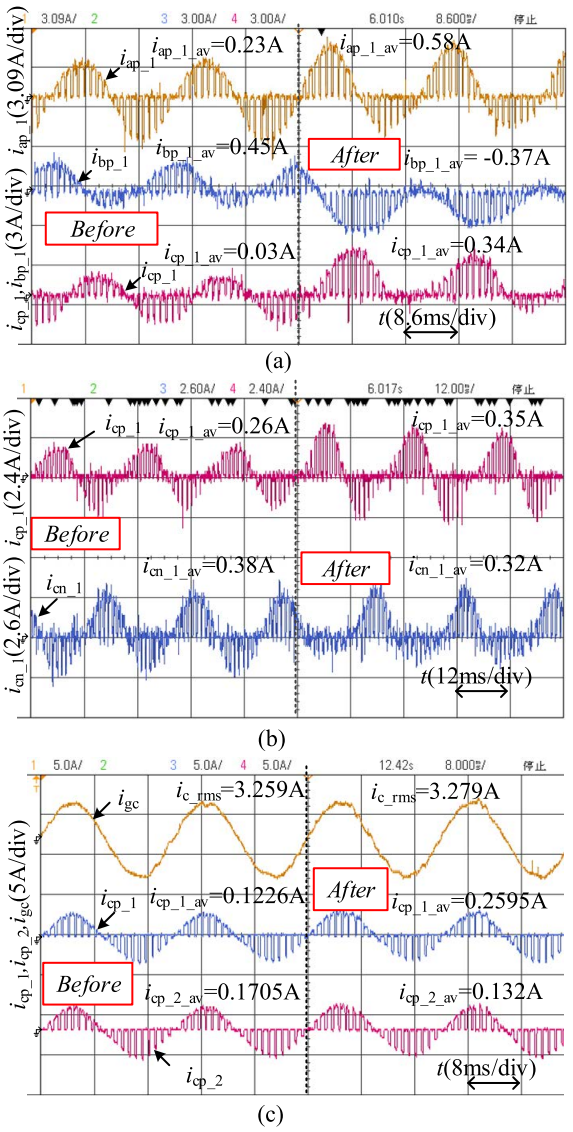

FIGURE 11. Experimental results of the three-layer balance control of SOC. (a) Different poles. (b) Upper and lower arms in phase C. (c) Two submodules in the upper arm of phase C.

First, the experiment of SOC balance control between different poles is carried out. It can be seen in Table.2 that at the beginning, the average value of SOC in each phase is ($\text{SOC}_\text{b} = 59.67\%$) > ($\text{SOC}_\text{c} = 48.61\%$) > ($\text{SOC}_\text{a} = 40.33\%$). The current waveforms of the energy storage unit in the upper arms are illustrated in Fig.11(a). After the first layer balance control strategy is employed, a positive DC current appears in phase A and phase C whose average SOC values are relatively smaller. While a negative DC current appears in phase B whose average SOC value is larger than phase A and phase C before balance control.

Before balance control, the average currents of the upper arms in each phase are calculated as 0.23A, 0.45A, and 0.03A. After implementing the first layer balance control

strategy, the average currents are 0.58A, −0.37A, and 0.34A. According to the change of average currents of each phase, it can be seen that positive DC circulating currents occur in phase A and phase C whose initial average SOC values are smaller, while a negative DC circulating current has occurred in phase B whose initial average SOC value is higher. Thus the energy is transferred from phase B to phase A and phase C, which proves the effectiveness of the SOC balance control between different poles.

Second, the experiment of SOC balance control between upper and lower arms in the same pole is carried out. It can be seen in Table.2 that, at the initial time, the SOC average value of the two submodules of the upper and lower arms in phase C is ($SOC_{cn} = 63.33\%$) > ($SOC_{cp} = 33.89\%$). On the basis of the first layer control, the second layer control is employed. The waveform of the energy storage unit current is shown in Fig.11(b), which was observed from the upper and lower arm submodules in phase C. It can be seen that the envelope of i_{cp_1} changes significantly while that of i_{cn_1} remains basically the same after implementing the balance control.

In Fig.11(b), the submodules' DC currents of the upper and lower arm in phase C are calculated as 0.26A, 0.38A, and the RMS values of the fundamental current are 1.47A and 1.7A respectively. After employing the second layer balance control strategy, the DC currents are 0.35A, 0.32A, and the RMS values of the fundamental currents are 1.84A and 1.52A respectively. As MMC-BESS is charging, the RMS value of the fundamental current in the upper arm increases after the second layer balance control strategy is employed while that in the lower arm decreases, indicating that the fundamental circulating current is negative at this time and the energy of lower arm flows into the upper arm. At the same time, the average value of the submodules' current in the upper arm becomes larger, which means its charging power also becomes larger. While the lower arm is just the opposite. That also indicates the energy of the lower arm is transferred to the upper arm, which proves the effectiveness of the SOC balance control between the upper and lower arms in the same pole.

Finally, the experiment of SOC balance control between submodules in the same arm is carried out. As seen in Table.2, it can be known that the SOC values of the two submodules in the upper arm in phase C are ($SOC_{cp\_1} = 4.44\%$) < ($SOC_{cp\_2} = 63.33\%$). Based on the first and second layer balance control, the third layer control is employed. The current waveforms of the two submodules' energy storage units in the upper arm of phase C are obtained and shown in Fig.11(c). From Fig.11(c), it can be seen that the current duty ratio of SM_1, which has a smaller SOC value than SM_2 before the third layer balance control, has increased, while the current duty ratio of SM_2 has decreased.

Before and after the third layer balance control strategy was implemented, the average current values of SM_1 and SM_2 changed from 0.1226A and 0.1705A to 0.2595A and 0.132A respectively, indicating that the charging power of SM_1 increased while the charging power of SM_2 decreased. The energy in the arm is transferred from SM_2 to SM_1, which proves the utility of SOC balance control between submodules in the same arm.

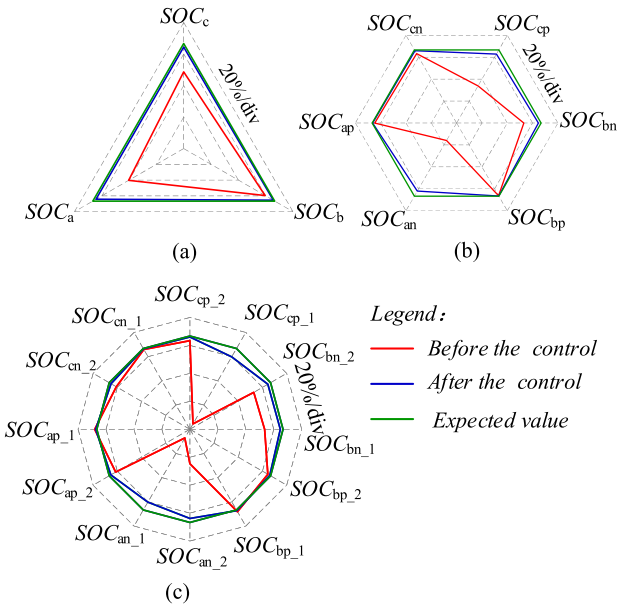

FIGURE 12. Radar chart of SOC values of batteries in MMC-BESS. (a) Different poles. (b) Upper and lower arms in the same pole. (c) Three-phase twelve submodules.

From the results listed in Table.2, the radar chart of the SOC values of the energy storage units at all layers before and after employing the three-layer balance control can be obtained, which is illustrated in Fig.12. The radar chart of the SOC values of different poles is shown in Fig.12(a), whose average value is 64.72%, which increases 130% compared with the initial value. Fig.12(b) represents the radar chart of the SOC values of the upper and lower arms in the same pole, whose average values are 64.23%, 65.59%, and 64.36% respectively, which increases 159%, 109%, and 132% respectively compared with the initial. Fig.12(c) expresses the radar chart of the SOC values of three-phase twelve submodules, and the average SOC of all submodules is 64.72%, which is an increase of 130% compared with the initial, and the standard deviation is 2.45, which is a decrease of 961%. It can be seen from Fig.12 that the implementation of three-layer balance control makes the SOC of each energy storage unit close to the expected value, which means the equilibrium effect is good. The standard deviation of SOC values is decreased, proving that the proposed control strategy is effective.

B. FLUCTUATING POWER SUPPRESSION

Assuming that the short-term grid-connected fluctuating power of the wind farm is given in Fig.13(a), which is also the high-frequency part of the wind farm's active power. The rated active power output by the wind farm is 200W, and the maximum fluctuating power in Fig.13(a) exceeds 50W, which is 0.25 p.u. Obviously, it is beyond the value of 0.1 p.u. specified by the standard [27].

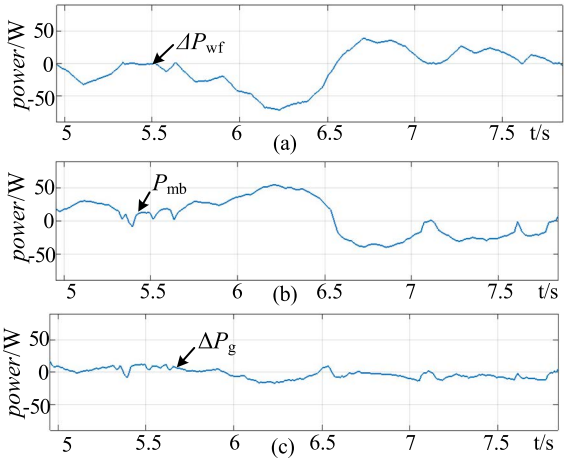

FIGURE 13. Fluctuating power suppression by MMC-BESS in the wind farm. (a) Simulated fluctuating power of wind farm. (b) Active power output by MMC-BESS. (c) Suppressed fluctuating power of wind farm.

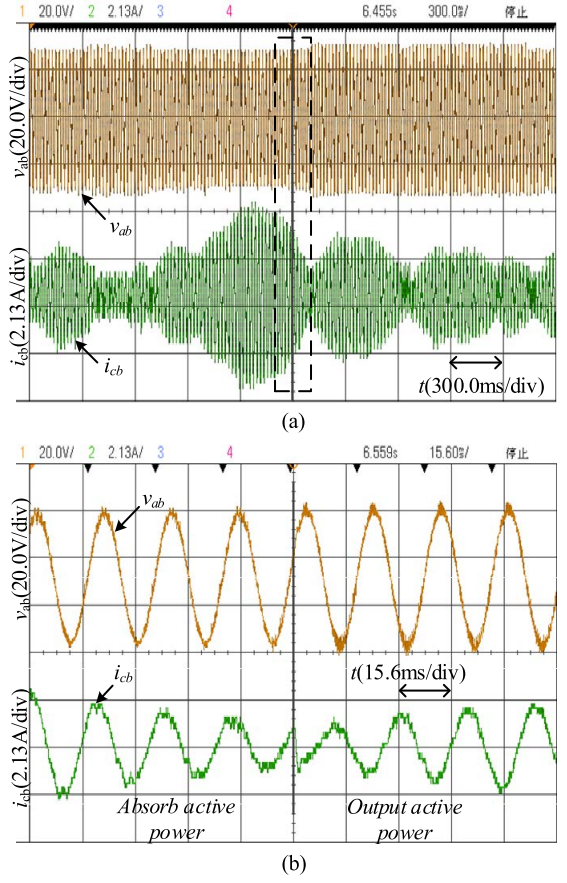

FIGURE 14. Dynamic waveforms of line voltage v_{ab} and phase current i_{cb} when employing fluctuating power suppression. (a) Line voltage v_{ab} and phase current i_{cb} waveform within 3 seconds. (b) Enlarged waveforms.

For the convenience of analysis, ΔP_{wf} is directly inverted as the output active power reference $P_{mb}*$ of MMC-BESS. The local load in Fig.5(a) is not considered, and the line inductor is 0.5mH to simulate the grid-connected wind farm. Fig.14(a) shows the dynamic waveform of line voltage v_{ab} and phase current i_{cb} when employing fluctuating power suppression strategy and Fig.14(b) is a partially enlarged waveform of Fig.14(a). From Fig.14(b), we can see that i_{cb} leads/lags v_{ab} 30° and 150°. Since the positive direction of the current is pointing to the PCC, it means MMC-BESS absorbs/emits active power to suppress fluctuating power output by the wind farm. The calculated instantaneous power P_{mb} of MMC-BESS is shown in Fig.13(b), ΔP_{wf} and P_{mb} are added to obtain the wind farm's fluctuating power after suppression. From Fig.13(c), it can be seen that MMC-BESS can smoothen the fluctuating power output by the wind farm quickly, and achieve peak-shaving and valley-filling of fluctuating power. The maximum fluctuating power within 1min in Fig.13(c) is 10W, i.e., 0.05 p.u., which is less than 0.1 p.u. and meets the standard.

C. PCC VOLTAGE REGULATION

As shown in Fig.5(a), the local load which is composed of Load A and Load B in the laboratory is considered, and the line inductor is 6mH. Then the load is switched on and off to simulate the PCC voltage fluctuation of the grid-connected wind farm.

First, the waveforms of v_{ab} and i_{ca} when PCC voltage drops are illustrated in Fig.15(a). As shown in Fig.15(a), only Load A is turned on during Δt_0, and the PCC line voltage is kept near the rated value through the voltage regulator. When load B is turned on during Δt_1, the PCC line voltage decreases 10.6% from 1.0 p.u. to 0.894 p.u. Then the MMC-BESS is put into operation. And the PCC voltage is adjusted during Δt_3, where the MMC-BESS works under capacitive conditions, and the PCC line voltage returns to 0.998 p.u., which means that the under-voltage is only 0.2%. Fig.15(b) shows the enlarged waveforms of PCC under-voltage adjustment. Since the positive direction of the compensation current points to the PCC, v_{ab} leads i_{ca} 122°, indicating that MMC-BESS is controlled as a capacitor to support PCC voltage.

Secondly, the waveforms of v_{ab} and i_{ca} are illustrated in Fig.15(c) when the PCC voltage rises. Load A and load B are turned on at the same time during Δt_0, and the PCC line voltage is maintained near the rated value through the voltage regulator. When load B is turned off during Δt_1, the PCC line voltage increases 13.0% from 1.0 p.u. to 1.13 p.u. Then the MMC-BESS is put into operation, and the PCC voltage is adjusted during Δt_3, where the MMC-BESS works under inductive conditions and the PCC line voltage return to 1.004 p.u., which means that the over-voltage is 0.4%. Fig.15(d) shows the enlarged waveforms of PCC over-voltage adjustment, v_{ab} lags i_{ca} 63°, indicating that the MMC-BESS is controlled as an inductor to reduce the PCC voltage.

It can be seen that MMC-BESS can adjust the PCC voltage well whether over/under voltage so that the PCC voltage fluctuation range is limited within the standard value, which meets the requirements of the standard [28]. The PCC voltage will decrease if the inductive load turns on, and it will rise if the load turns off, while the capacitive load will be the opposite. Through the proposed PCC voltage regulation strategy illustrated above, the MMC-BESS is controlled as a

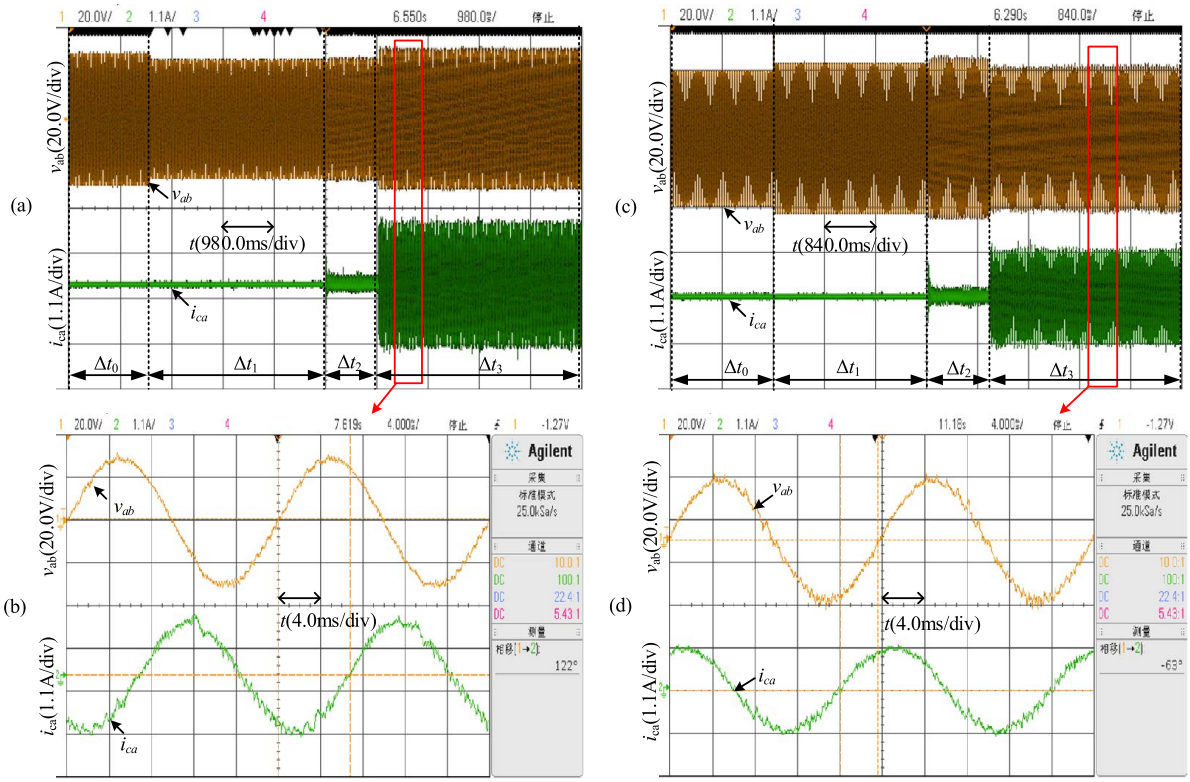

FIGURE 15. Dynamic waveforms of line voltage v_{ab} and phase current i_{ca} when employing PCC voltage regulation. (a) Under-voltage regulation. (b) Enlarged waveforms when MMC-BESS works as a capacitor. (c) Over-voltage regulation. (d) Enlarged waveforms when MMC-BESS works as an inductor.

capacitor or inductor, and the PCC voltage fluctuation range can be limited to ±5% of the rated value.

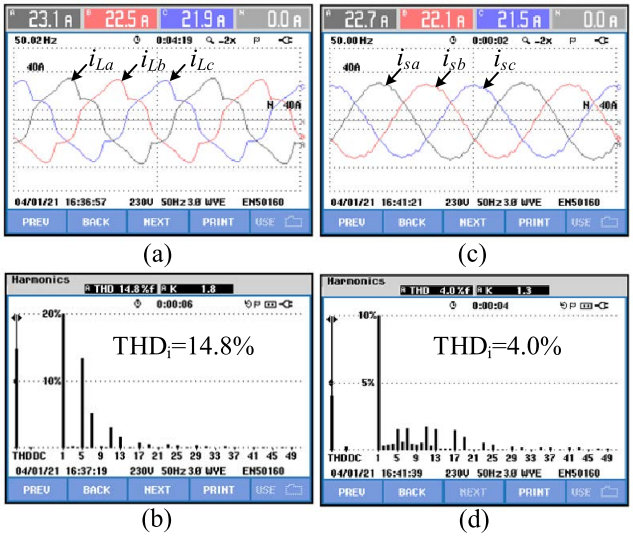

FIGURE 16. Steady-state experimental results of harmonic mitigation by the prototype. (a) Load currents. (b) Spectrum of load currents. (c) Grid currents. (d) Spectrum of grid currents.

D. HARMONIC MITIGATION

Both Load C and Load D are turned on to simulate harmonic pollution in the grid-connected wind farm, whose parameters

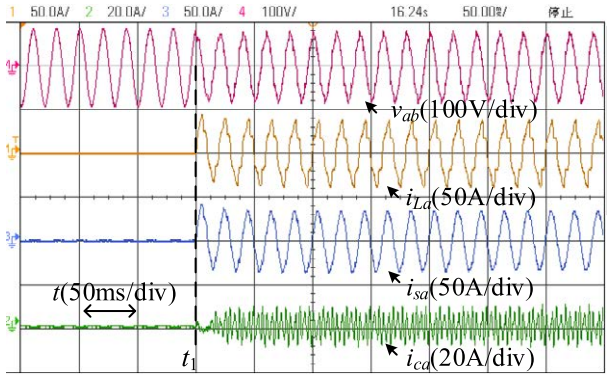

FIGURE 17. Dynamic experimental results of harmonic mitigation by the prototype.

are listed in Table.1. As shown in Fig.16(a), the load currents i_L is distorted severely and the THD of i_{La} is 14.8%. Before the harmonic mitigation control strategy is implemented, the grid currents i_s is equal to i_L. Therefore, the THD of i_{sa} is also 14.8%, which cannot meet the limits of the IEEE std.519-2014 [29].

The results of applying the proposed harmonic mitigation strategy with the prototype are shown in Fig.16(c) and (d). As mentioned before, due to the limitation of equivalent switching frequency, the prototype only suppresses the 5^{th}, 7^{th}, and 11^{th} harmonics selectively. It can be seen from Fig.16(c) that after applying the harmonic mitigation strategy

by the prototype, the waveform of grid currents i_s is almost sinusoidal. The THD of i_{sa} is reduced from 14.8% to 4.0%, which can meet the standard [29].

The dynamic waveform of harmonic mitigation is shown in Fig.17. Both Load C and Load D are turned on at t_1. With the proposed harmonic mitigation strategy, the prototype outputs harmonic suppression currents quickly to keep grid currents sinusoidal. Hence, through the proposed harmonic mitigation strategy by MMC-BESS, the harmonic pollution in the grid-connected wind farm can be alleviated, and the power quality can be further improved.

VI. CONCLUSION

Aiming at the power fluctuation, PCC voltage instability, and harmonic pollution in distributed power generation systems, the MMC-BESS applied in the grid-connected wind farm is analyzed. Compared with using energy storage devices, reactive power compensation apparatus, and active power filters to deal with the above problems individually, MMC-BESS integrates active and reactive power compensation ability simultaneously, which can realize power fluctuation suppression, PCC voltage regulation, and harmonic mitigation at the same time. Hence, the overall control strategy of MMC-BESS applied in the grid-connected wind farm is proposed. Besides, due to the SOC unbalance during the operation of MMC-BESS, the three-layer balance control of SOC is proposed accordingly. In order to validate the effectiveness and feasibility of the proposed strategy, plenty of experimental results are obtained from a downscaled three-phase twelve submodules MMC-BESS. And the conclusions can be summarized as follows:

(i) After applying the three-layer balance control of SOC, the standard deviation of SOC values among all submodules is reduced from 23.55 to 2.45, which means the equilibrium effect is good.

(ii) With fluctuating power suppression strategy, the maximum fluctuating power within 1 min in the simulated grid-connected wind farm is 0.05 p.u., which is less than 0.1 p.u. and meets the requirements of the technical rule for active power regulation and control of wind farm.

(iii) Through detecting the PCC voltage and controlling the reactive power injected from MMC-BESS to the PCC, the fluctuation of PCC voltage is limited to the specified range, which meets the requirements of the power quality of wind turbines generator systems.

(iv) By suppressing 5^{th}, 7^{th}, and 11^{th} harmonic currents in the nonlinear load currents selectively based on the proposed harmonic mitigation strategy, the THD of grid currents is reduced from 14.8% to 4.0%, which can meet the limits of the IEEE Std.519-2014.

By adjusting the number of submodules and batteries, the voltage level of MMC-BESS is increased. Therefore, the proposed balance control of SOC for MMC-BESS with power fluctuation suppression, PCC voltage regulation, and harmonic mitigation is applicable in actual wind farms.

REFERENCES

[1] E. Du, N. Zhang, B.-M. Hodge, Q. Wang, C. Kang, B. Kroposki, and Q. Xia, "The role of concentrating solar power toward high renewable energy penetrated power systems," *IEEE Trans. Power Syst.*, vol. 33, no. 6, pp. 6630–6641, Nov. 2018.

[2] A. Jahid, M. K. H. Monju, M. E. Hossain, and M. F. Hossain, "Renewable energy assisted cost aware sustainable off-grid base stations with energy cooperation," *IEEE Access*, vol. 6, pp. 60900–60920, 2018.

[3] J. Ouyang, M. Li, Z. Zhang, and T. Tang, "Multi-timescale active and reactive power-coordinated control of large-scale wind integrated power system for severe wind speed fluctuation," *IEEE Access*, vol. 7, pp. 51201–51210, 2019.

[4] Q. Tabart, I. Vechiu, A. Etxeberria, and S. Bacha, "Hybrid energy storage system microgrids integration for power quality improvement using four-leg three-level NPC inverter and second-order sliding mode control," *IEEE Trans. Ind. Electron.*, vol. 65, no. 1, pp. 424–435, Jan. 2018.

[5] X. Han, Y. Qu, P. Wang, and J. Yang, "Four-dimensional wind speed model for adequacy assessment of power systems with wind farms," *IEEE Trans. Power Syst.*, vol. 28, no. 3, pp. 2978–2985, Aug. 2013.

[6] S. Ghosh and S. Kamalasadan, "An energy function-based optimal control strategy for output stabilization of integrated DFIG-flywheel energy storage system," *IEEE Trans. Smart Grid*, vol. 8, no. 4, pp. 1922–1931, Jul. 2017.

[7] F. Islam, A. Al-Durra, and S. M. Muyeen, "Smoothing of wind farm output by prediction and supervisory-control-unit-based FESS," *IEEE Trans. Sustain. Energy*, vol. 4, no. 4, pp. 925–933, Oct. 2013.

[8] A. Esmaili, B. Novakovic, A. Nasiri, and O. Abdel-Baqi, "A hybrid system of li-ion capacitors and flow battery for dynamic wind energy support," *IEEE Trans. Ind. Appl.*, vol. 49, no. 4, pp. 1649–1657, Jul. 2013.

[9] H. Lee, B. Y. Shin, S. Han, S. Jung, B. Park, and G. Jang, "Compensation for the power fluctuation of the large scale wind farm using hybrid energy storage applications," *IEEE Trans. Appl. Supercond.*, vol. 22, no. 3, Jun. 2012, Art. no. 5701904.

[10] J. Qi, W. Zhao, and X. Bian, "Comparative study of SVC and STATCOM reactive power compensation for prosumer microgrids with DFIG-based wind farm integration," *IEEE Access*, vol. 8, pp. 209878–209885, 2020.

[11] A. Choudhury, P. Pillay, and S. S. Williamson, "Comparative analysis between two-level and three-level DC/AC electric vehicle traction inverters using a novel DC-link voltage balancing algorithm," *IEEE J. Emerg. Sel. Topics Power Electron.*, vol. 2, no. 3, pp. 529–540, Sep. 2014.

[12] C. Xu, K. Dai, X. Chen, and Y. Kang, "Voltage droop control at point of common coupling with arm current and capacitor voltage analysis for distribution static synchronous compensator based on modular multilevel converter," *IET Power Electron.*, vol. 9, no. 8, pp. 1643–1653, Jun. 2016.

[13] C. Xu, K. Dai, X. Chen, and Y. Kang, "Unbalanced PCC voltage regulation with positive- and negative-sequence compensation tactics for MMC-DSTATCOM," *IET Power Electron.*, vol. 9, no. 15, pp. 2846–2858, Dec. 2016.

[14] S. Debnath, J. Qin, B. Bahrani, M. Saeedifard, and P. Barbosa, "Operation, control, and applications of the modular multilevel converter: A review," *IEEE Trans. Power Electron.*, vol. 30, no. 1, pp. 37–53, Jan. 2015.

[15] I. Trintis, S. Munk-Nielsen, and R. Teodorescu, "A new modular multilevel converter with integrated energy storage," in *Proc. 37th Annu. Conf. IEEE Ind. Electron. Soc.*, Nov. 2011, pp. 1075–1080.

[16] T. Soong and P. W. Lehn, "Evaluation of emerging modular multilevel converters for BESS applications," *IEEE Trans. Power Del.*, vol. 29, no. 5, pp. 2086–2094, Oct. 2014.

[17] M. Vasiladiotis and A. Rufer, "Analysis and control of modular multilevel converters with integrated battery energy storage," *IEEE Trans. Power Electron.*, vol. 30, no. 1, pp. 163–175, Jan. 2015.

[18] Q. Chen, R. Li, and X. Cai, "Analysis and fault control of hybrid modular multilevel converter with integrated battery energy storage system," *IEEE J. Emerg. Sel. Topics Power Electron.*, vol. 5, no. 1, pp. 64–78, Mar. 2017.

[19] L. Baruschka and A. Mertens, "Comparison of cascaded H-bridge and modular multilevel converters for BESS application," in *Proc. IEEE Energy Convers. Congr. Expo.*, Sep. 2011, pp. 909–916.

[20] A. Hillers and J. Biela, "Optimal design of the modular multilevel converter for an energy storage system based on split batteries," in *Proc. 15th Eur. Conf. Power Electron. Appl. (EPE)*, Sep. 2013, pp. 1–11.

[21] H. P. Mohammadi and M. T. Bina, "A transformerless medium-voltage STATCOM topology based on extended modular multilevel converters," *IEEE Trans. Power Electron.*, vol. 26, no. 5, pp. 1534–1545, May 2011.

[22] M. Schroeder, S. Henninger, J. Jaeger, A. Ras, H. Rubenbauer, and H. Leu, "Integration of batteries into a modular multilevel converter," in *Proc. 15th Eur. Conf. Power Electron. Appl. (EPE)*, Sep. 2013, pp. 1–12.
[23] D. M. Rosewater, D. A. Copp, T. A. Nguyen, R. H. Byrne, and S. Santoso, "Battery energy storage models for optimal control," *IEEE Access*, vol. 7, pp. 178357–178391, 2019.
[24] J. Hu, K. Xu, L. Lin, and R. Zeng, "Analysis and enhanced control of hybrid-MMC-based HVDC systems during asymmetrical DC voltage faults," *IEEE Trans. Power Del.*, vol. 32, no. 3, pp. 1394–1403, Jun. 2017.
[25] Y. Zhang, K. Dai, C. Xu, Y. Kang, and Z. Dai, "Multiple sampling PSC-PWM with hierarchical control architecture for MMC-DSTATCOM," *IET Electr. Power Appl.*, vol. 13, no. 10, pp. 1431–1440, Oct. 2019.
[26] B. Yang, K. Dai, C. Yang, H. Luo, K. He, and Z. Dai, "Improvement of recursive DFT for APF with higher switching frequency to suppress wideband harmonics," *IEEE Access*, vol. 9, pp. 144300–144312, 2021.
[27] *Energy Industry Standard of the People's Republic of China, Technical Rule for Active Power Regulation and Control of Wind Farm*, document NB/T 31110-2017, 2017.
[28] *National Standard of the People's Republic of China, Measurement and Assessment of Power Quality Characteristics of Wind Turbines Generator Systems*, document GB/T 20320-2013, 2013.
[29] *IEEE Recommended Practice and Requirements for Harmonic Control in Electric Power Systems*, IEEE Standard 519-2014, 2014.

HUI LUO was born in Jiangxi, China, in 1998. He received the B.S. degree in electrical engineering from Central South University (CSU), Changsha, China, in 2020. He is currently pursuing the M.S. degree in electrical engineering with the Huazhong University of Science and Technology (HUST), Wuhan, China. His research interests include power quality control, active power filter, MMC-BESS, and modeling and stability analysis of inverters.

CHEN XU (Member, IEEE) was born in Hubei, China, in 1988. He received the B.S. degree in electrical engineering from the School of Electrical and Electronic Engineering (SEEE), Huazhong University of Science and Technology (HUST), Wuhan, China, in 2010, and the Ph.D. degree in power electronics from the Department of Applied Electronics (DAE), HUST, in 2016. From October 2016 to September 2020, he was working as a Postdoctoral Fellow and a Research Assistant with DAE, HUST. Since October 2020, he has been a Research Fellow with the Department of Electrical Engineering, Eindhoven University of Technology, Eindhoven, The Netherlands. Since December 2021, he has been an Associate Professor with the Department of Electrical Engineering, School of Mechatronic Engineering and Automation, Shanghai University, Shanghai, China. His research interests include flexible AC and DC transmission and distribution technology, power quality control, multilevel converter, and power supply system for hydrogen production from water electrolysis.

KE DAI was born in Hubei, China, in 1969. He received the B.S. degree in electrical engineering from the Huazhong University of Science and Technology (HUST), Wuhan, China, in 1990, the M.S. degree in industrial automation from the Wuhan University of Technology, in 1998, and the Ph.D. degree from HUST, in 2003.

From 1990 to 1995, he was an Electrical Assistant Engineer with the Wuhan Marine Electric Propulsion Institute. In 1998, he joined the Department of Applied Electronics, HUST, as a Lecturer, where he became an Associate Professor, in 2004. From 2012 to 2013, he was a Visiting Scholar at the Department of Electrical Engineering and Computer Science, University of Tennessee, Knoxville, TN, USA. He is the author or coauthor of more than 100 technical papers published in journals and conference proceedings. His research interests include static chopper, converter and inverter, reactive power compensator, active power filter, uninterruptible power supply, universal power quality conditioner, unified power flow controller, power electronic system stability and power quality, renewable energy, distributed generation, and smart grid. He is the corresponding author of this article.

CONGZHI CHENG was born in Anhui, China, in 1995. He received the B.S. degree in electrical engineering from the China University of Mining and Technology (CUMT), Xuzhou, China, in 2017, and the M.S. degree in electrical engineering from the Huazhong University of Science and Technology (HUST), Wuhan, China, in 2021. He is currently working at Huawei Technologies Company Ltd. His research interests include power quality control, active power filter, and modeling of multilevel converter.

YONGSHUO HUANG was born in Guangxi, China, in 1992. He received the M.S. degree in electrical engineering from the Huazhong University of Science and Technology (HUST), Wuhan, China, in 2019. He is currently working with Nanning Power Supply Bureau of Guangxi Power Grid Company Ltd., Nanning, Guangxi, China. His research interests include power quality control, relay protection, and modeling and stability analysis of grid-connected converters.

FEI PAN was born in Hubei, China, in 1979. He received the B.S. degree in electronic and information engineering from the Huazhong University of Science and Technology (HUST), Wuhan, China, in 2001, the M.S. degree in computer science from Bowling Green State University, in 2003, and the M.S. degree in industrial engineering and the Ph.D. degree in management from Purdue University, in 2004 and 2009, respectively. He is currently working at Shanghai Surpass Sun Electric Company Ltd.